

# Control and Characterization of Organic Solar Cell Morphology Through Variable-Pressure Solvent Vapor Annealing

Derek Zomerman,<sup>†</sup> Jessica Kong,<sup>‡</sup> Seth M. McAfee,<sup>§</sup> Gregory C. Welch,<sup>§</sup> and Timothy L. Kelly\*,<sup>†</sup>

<sup>†</sup>Department of Chemistry, University of Saskatchewan, 110 Science Place, Saskatoon, Saskatchewan S7N 5C9, Canada

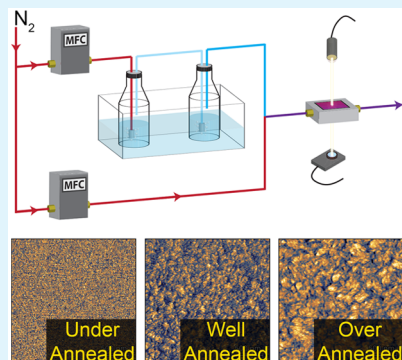
<sup>‡</sup>Department of Chemistry, University of Washington, Seattle, Washington 98195-1700, United States

<sup>§</sup>Department of Chemistry, University of Calgary, 731 Campus Place N.W., Calgary, Alberta T2N 1N4, Canada

## S Supporting Information

**ABSTRACT:** Solvent vapor annealing (SVA) of organic photovoltaics (OPVs) has become an important postdeposition treatment, but current OPV SVA methods are difficult to reproduce and neither tunable nor scalable. Herein, it is shown that a variable-pressure solvent vapor annealing (VP-SVA) system can be used to reproducibly and tunably anneal OPV active layers to produce highly controlled film morphologies. We show that VP-SVA is useful not only for the well-studied P3HT:PC<sub>61</sub>BM model system, but also for modern OPV active layers based on nonfullerene acceptors. Phase separation and material crystallinity are precisely tuned by controlling the solvent vapor concentration used during the annealing process, as evidenced by photoinduced force microscopy (PiFM) and grazing incidence wide-angle X-ray scattering (GIWAXS). The results show that overannealing occurs at saturated solvent vapor pressures, highlighting the importance of the VP-SVA technique.

**KEYWORDS:** organic photovoltaics, bulk heterojunctions, morphology control, solvent vapor annealing, photoinduced force microscopy



## INTRODUCTION

Organic photovoltaics (OPVs) are in the early stages of commercialization because of recent advances in OPV performance. The most common architecture for these devices is the bulk heterojunction (BHJ), which is an intimate mixture of an electron donor and an electron acceptor. Device performance is inextricably linked to the morphology of the BHJ; if domain sizes are either too large or too small, recombination losses become high and the device performance suffers.<sup>1–3</sup> Therefore, a huge amount of effort has been put into morphology control in OPVs.<sup>1,4–10</sup>

Common methods for controlling the BHJ morphology are through solvent selection, solvent additives, thermal annealing, and solvent vapor annealing (SVA).<sup>1</sup> Choosing a casting solvent with a higher boiling point allows the BHJ materials more time to self-assemble, although a limited number of solvent choices makes it difficult to fine-tune this parameter. High-boiling-solvent additives such as 1,8-diiodooctane (DIO) are also a common way of slowing the drying process; however, DIO can degrade OPV materials if not removed under high vacuum,<sup>11–13</sup> a step which is ideally avoided in high throughput processing. Thermal annealing heats the materials past their glass transition temperature, allowing the film to reorganize into a more thermodynamically stable state. The degree of thermal annealing can be varied by changing the annealing temperature and duration, allowing it to be optimized independently of the solvent system; however, it is

an energy intensive processing step, and the high temperatures can potentially degrade other device components.

In contrast, SVA involves no thermal load, making it an excellent postdeposition processing method. The simplest SVA method is the “bell jar” approach.<sup>6,7,14–18</sup> The OPV active layer is placed on a support in a sealed jar containing a small amount of solvent. The solvent vapor partially solvates the BHJ film, allowing it to rearrange to a more thermodynamically favorable morphology.<sup>4,19–21</sup> Unfortunately, this method is difficult to reproduce without knowing the exact size and shape of the jar, the height of the film support, and the volume of solvent used. Additionally, control over the solvent vapor concentration and the processing times (both annealing and drying) is lacking. An improvement to the bell jar method uses a vertical tube that is open at the top and sealed at the bottom.<sup>17,22–27</sup> Solvent is added to the bottom of the tube, and through evaporation and diffusion, a concentration gradient of solvent vapor develops in the tube. This allows for variable-pressure solvent vapor annealing (VP-SVA), but it takes several hours for the solvent vapor pressure to equilibrate, and it is inherently a small batch process. This makes it unsuitable for industrial development.

Received: July 23, 2018

Accepted: September 14, 2018

Published: September 14, 2018

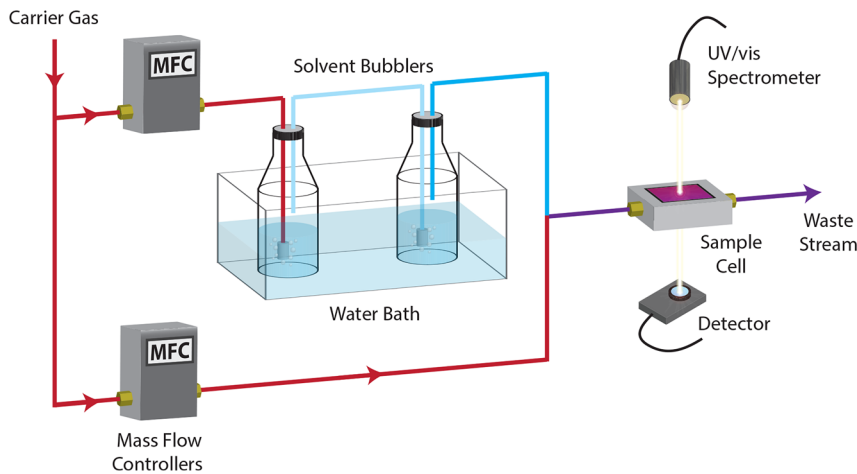
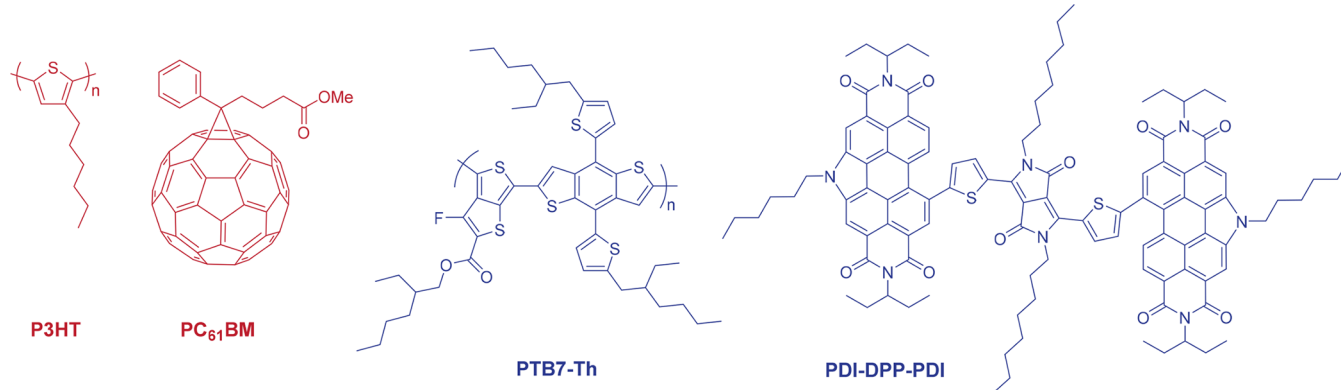


**Figure 1.** Schematic of the VP-SVA system used in this study.

**Chart 1. Two OPV Active Layer Systems: P3HT:PC<sub>61</sub>BM and PTB7-Th:PDI-DPP-PDI**



As an alternative, flow-through SVA methods have been developed, primarily by researchers in the field of block copolymer self-assembly.<sup>14,15,28–39</sup> The flow through method increases the reproducibility, precision, and scalability of the annealing process by allowing solvent vapor pressures, wetting and drying times, and flow rates to all be individually controlled and tailored to the specific system under study. This type of VP-SVA system works by splitting a stream of dry carrier gas and sending it to two (or more) flow controllers (Figure 1). One gas stream remains dry, while the other stream passes through solvent bubblers, becoming saturated in solvent vapor ( $p_{\text{sat}}$ ). The ratio of the two flow rates controls the dilution factor and therefore the partial pressure of solvent vapor used for annealing ( $p$ ). Such a system can be expanded to accommodate multiple bubblers with different solvents, allowing specific copolymer blocks or BHJ components to be annealed simultaneously.<sup>1,33</sup> However, despite the success of VP-SVA in the field of block copolymers, few reports have used such an annealing process to control BHJ morphology.<sup>4,19,40–42</sup>

Herein, BHJ blends were annealed with a flow through VP-SVA system, and the effect of solvent vapor pressure on BHJ morphology, crystallinity, and device performance was examined. For this study two different active layers were investigated: P3HT:PC<sub>61</sub>BM, and PTB7-Th:PDI-DPP-PDI (Chart 1). P3HT:PC<sub>61</sub>BM is an extremely well-studied BHJ blend,<sup>4,23,25,43–49</sup> making it an excellent model system with which to study the VP-SVA method. PTB7-Th:PDI-DPP-PDI

was chosen to be representative of more modern OPV systems, as it contains a less ordered donor polymer (PTB7-Th) and a nonfullerene electron acceptor (PDI-DPP-PDI).<sup>6,50–52</sup> Additionally, the PTB7-Th:PDI-DPP-PDI system is known to overanneal,<sup>6</sup> making it particularly suitable to the VP-SVA approach. It is shown that by varying the concentration of chloroform vapor used during the annealing process, both the crystallinity and the degree of phase separation in the BHJ film can be precisely tailored, as evidenced by UV/vis spectroscopy, grazing incidence wide-angle X-ray scattering (GIWAXS), and photoinduced force microscopy (PiFM). We also show that these changes in film morphology can be correlated to changes in device performance. Critically, the best results are achieved with subsaturation vapor pressures, highlighting the importance of the VP-SVA approach in device optimization.

## RESULTS AND DISCUSSION

**P3HT:PC<sub>61</sub>BM. UV/Visible Spectroscopy.** The VP-SVA system (Figure 1) was designed such that UV/vis spectroscopy could be performed *in situ* on thin films during the SVA process. Since the absorbance spectra of P3HT are highly sensitive to polymer aggregation and crystallinity,<sup>44</sup> this provides an excellent probe of morphological rearrangement occurring during SVA. We therefore performed *in situ* UV/vis spectroscopy on P3HT:PC<sub>61</sub>BM thin films (cast from chloroform) as they were annealed in varying concentrations of chloroform vapor. Samples were purged with dry nitrogen for 2 min, followed by 30 min of solvent annealing and 30 min

of purging with nitrogen. Spectra were acquired every 2 min during this process (Figure S1). For the as cast P3HT:PC<sub>61</sub>BM film, the UV/vis spectrum consists of a single broad absorption band at 503 nm (Figure 2a), indicating a low degree of

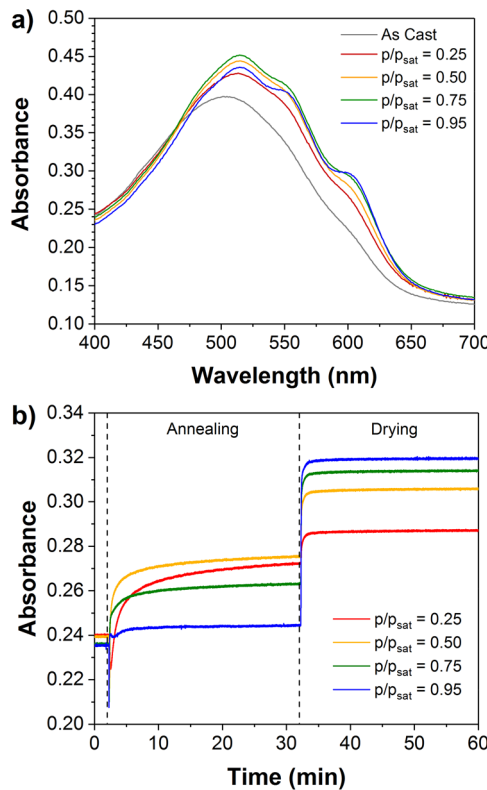


**Figure 2.** (a) Post-annealing UV/vis spectra and (b) absorbance at 600 nm as a function of time for P3HT:PC<sub>61</sub>BM thin films annealed at various chloroform vapor concentrations.

aggregation due to the kinetic trapping of amorphous P3HT. As the films are annealed at progressively higher chloroform

concentrations ( $p/p_{\text{sat}} = 0.25, 0.50, 0.75$ , and  $0.95$ ), prominent vibronic shoulders grow in at 548 and 600 nm, indicating the aggregation and crystallization of the P3HT chains.<sup>43</sup>

To increase the temporal resolution of the annealing experiment, we monitored the absorbance at 600 nm as P3HT:PC<sub>61</sub>BM thin films were annealed at various chloroform concentrations (Figure 2b). The annealing experiment was conducted in the same way as before: the sample was purged with dry nitrogen for 2 min, followed by 30 min of SVA and 30 min of purging with nitrogen. For the first minute of SVA, the absorbance at 600 nm decreased slightly, regardless of chloroform concentration. This is consistent with a slight reduction in the degree of aggregation as the film initially swells with solvent.<sup>19</sup> After this initial swelling, the absorbance at 600 nm increases for the remainder of the solvent treatment as the polymer chains rearrange and begin to aggregate. This effect is most pronounced for the lower solvent concentrations ( $p/p_{\text{sat}} = 0.25, 0.50$ ), as at the highest concentrations ( $p/p_{\text{sat}} = 0.75, 0.95$ ) the film is highly swollen with solvent and aggregation is more limited. As soon as the solvent flow is removed, however, the films deswell and show a rapid increase in absorbance as the P3HT aggregates. The degree of aggregation (as evidenced by the overall change in absorbance at 600 nm) depends on the concentration of chloroform vapor used during annealing, with higher solvent partial pressures leading to greater overall crystallization of the film. Importantly, the in situ absorbance measurements (Figure 2b) demonstrate that the degree of crystallization depends mainly on the solvent partial pressure ( $p/p_{\text{sat}}$ ) and is largely independent of the annealing time (with the exception of  $p/p_{\text{sat}} = 0.25$ ); this makes it substantially easier to reproducibly control the degree of annealing and limit overannealing of the films.

**Photoinduced Force Microscopy.** Since film morphology has a substantial impact on the performance of OPV devices, evaluating the degree of phase separation in BHJ blends is extremely important in device optimization. Traditionally, atomic force microscopy (AFM) has used height and phase

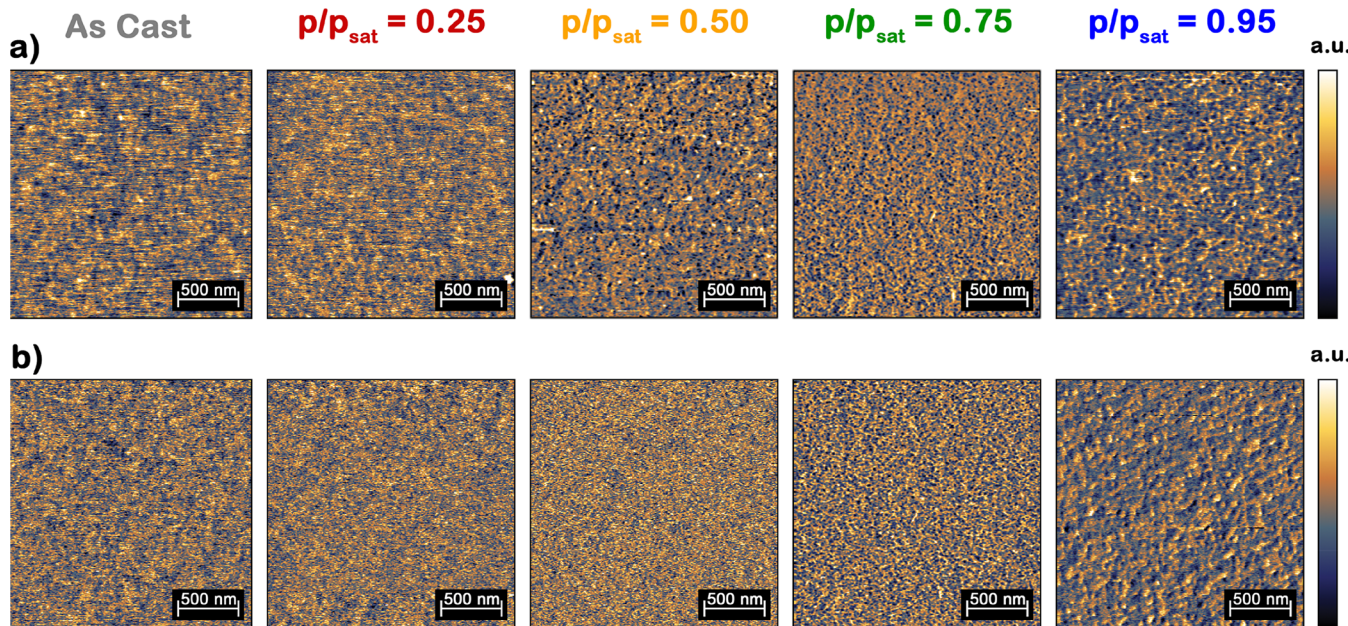


**Figure 3.** PiFM images of P3HT:PC<sub>61</sub>BM thin films annealed at various chloroform vapor concentrations. Excitation at (a) 810 and (b) 1740 cm<sup>-1</sup>.

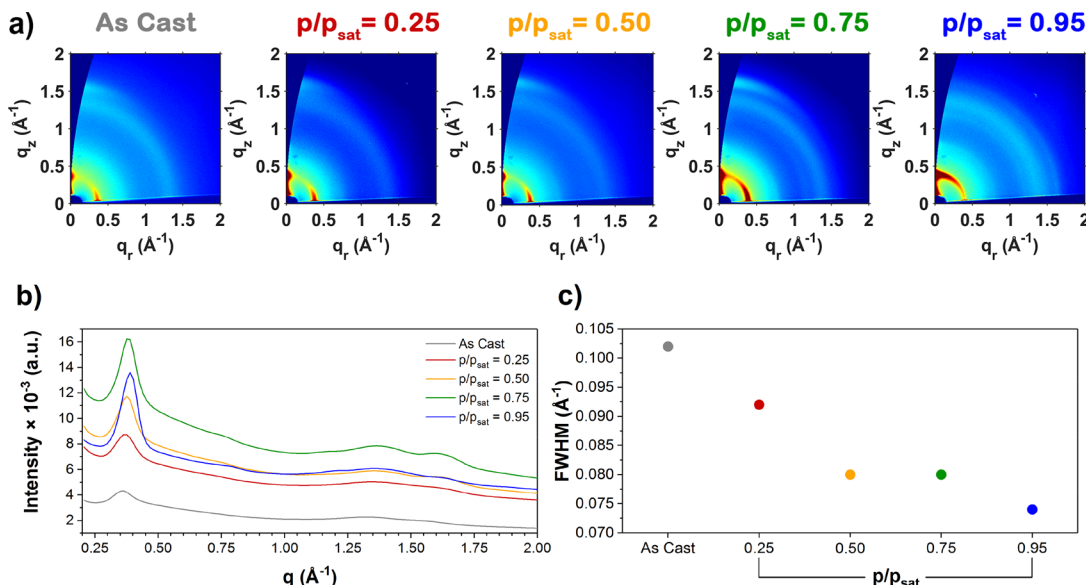


**Figure 4.** (a) GIWAXS patterns of P3HT:PC<sub>61</sub>BM thin films annealed at various chloroform vapor concentrations. (b) Azimuthally integrated linecuts (from  $\chi = -85^\circ$  to  $85^\circ$ ) of the GIWAXS patterns from panel a. (c) Full-width-at-half-maximum (fwhm) of the P3HT (100) peaks after background subtraction.

information to tangentially identify phase domains, based on either topographic features or the Young's modulus, respectively.<sup>53–55</sup> More recently, the development of PiFM has allowed phase domains in both block copolymers and BHJ films to be imaged directly, based on their IR absorbance spectra.<sup>53,56</sup> We therefore employed PiFM to examine the morphology of P3HT:PC<sub>61</sub>BM thin films, both as cast and after annealing at various chloroform vapor concentrations (Figure 3); topographic AFM images are shown in Figure S2 for comparison. The PiFM imaging of P3HT was performed at 810 cm<sup>-1</sup>, which corresponds to an out-of-plane C–H bending mode of the thiophene rings;<sup>57</sup> PiFM imaging of PC<sub>61</sub>BM was carried out at 1740 cm<sup>-1</sup>, corresponding to the carbonyl stretching mode of the methyl ester (Figure S3). Importantly, each of these vibrational modes is unique to the specific BHJ component, allowing the phase domains to be unambiguously identified in the PiFM imaging. For the as cast film, there is little apparent contrast in both PiFM images (810 and 1740 cm<sup>-1</sup>), and the images consist primarily of noise. This indicates that the two components of the BHJ are roughly homogeneously distributed within the film, as expected for a P3HT:PC<sub>61</sub>BM film spin coated from chloroform. Annealing at  $p/p_{\text{sat}} = 0.25$  does not materially change the distribution of the two components, with poor contrast and noisy images indicating a homogeneous distribution of P3HT and PC<sub>61</sub>BM. After annealing at  $p/p_{\text{sat}} = 0.50$ , distinct domains of P3HT begin to appear in the 810 cm<sup>-1</sup> PiFM image; however, the PC<sub>61</sub>BM does not display the same level of phase separation, as noted by the 1740 cm<sup>-1</sup> PiFM image. By  $p/p_{\text{sat}} = 0.75$ , both PiFM images show clear signs of phase separation, and the BHJ morphology consists of small, interconnected domains of P3HT and PC<sub>61</sub>BM. These domains then grow in size after annealing at  $p/p_{\text{sat}} = 0.95$ , producing nanoscale PC<sub>61</sub>BM globules surrounded by a P3HT network.

The same trends observed directly in the PiFM images are also evident in the fast Fourier transform (FFT) of the images. In the FFT of the 810 cm<sup>-1</sup> PiFM data (Figure S4a), both the as cast and  $p/p_{\text{sat}} = 0.25$  annealed films are dominated by a pronounced vertical stripe (indicating periodicity along the

slow axis of the scan); the image is dominated by line-scan noise. This noise disappears at  $p/p_{\text{sat}} = 0.50$ , and as the annealing partial pressure is increased, the distribution of spatial frequencies collapses toward the low frequency regime, indicative of the growth of larger domains in the image. This behavior is mirrored in the FFT of the 1740 cm<sup>-1</sup> PiFM data (Figure S4b), with the exception that the  $p/p_{\text{sat}} = 0.50$  FFT still shows a wide distribution of spatial frequencies and evidence of line-scan noise, consistent with the lack of phase separation observed in the 1740 cm<sup>-1</sup> PiFM image. However, both the  $p/p_{\text{sat}} = 0.75$  and 0.95 FFT images show the expected trend toward low spatial frequencies, indicative of extensive phase separation in the P3HT:PC<sub>61</sub>BM blend.

These same trends can still be observed, albeit less clearly, in the topographic AFM data (Figure S2). The as cast film has a nanoscale surface roughness ( $R_q = 0.58$  nm) typical for many spin coated films of organic materials; however, as evidenced by the PiFM data, this is not indicative of any substantial degree of phase separation. When the films are annealed at the lower concentrations of chloroform vapor ( $p/p_{\text{sat}} = 0.25, 0.50, 0.75$ ), there is little change in the  $R_q$  (0.68, 0.56, and 0.80 nm, respectively); however, when the film is annealed at the highest chloroform concentration ( $p/p_{\text{sat}} = 0.95$ ), there is a marked increase in surface roughness ( $R_q = 1.99$  nm). While the  $R_q$  of the topographic AFM data appears to be correlated with the degree of phase separation, and can provide a relative comparison between closely related films, the PiFM images depict the degree of phase separation much more clearly.

**Grazing Incidence Wide-Angle X-ray Scattering.** Since charge transport is strongly affected by the degree of crystallinity in organic semiconductors,<sup>58</sup> we used grazing incidence wide-angle X-ray scattering (GIWAXS) to probe the effect of VP-SVA on the crystallinity of the P3HT:PC<sub>61</sub>BM thin films (Figure 4a). The GIWAXS pattern of the as cast film shows a P3HT (100) peak at  $q \approx 0.35$  Å<sup>-1</sup>; the pronounced intensity along the  $q_r$  axis indicates some degree of preferential face-on orientation.<sup>4,59</sup> This can be better visualized in the azimuthally integrated linecuts between  $\chi = 0$ – $20^\circ$  and  $70$ – $90^\circ$  (Figure S5). The GIWAXS pattern also contained a broad

P3HT (010)  $\pi$ - $\pi$  stacking peak at  $q \approx 1.6 \text{ \AA}^{-1}$ ; this was oriented along the  $q_z$  axis, further indicating a preference for face-on orientation of the P3HT.<sup>4</sup> The broad ring at  $q \approx 1.3 \text{ \AA}^{-1}$  is due to the PC<sub>61</sub>BM and is mostly isotropic, indicating little-to-no preference in PC<sub>61</sub>BM orientation.<sup>4</sup>

The P3HT:PC<sub>61</sub>BM films annealed at chloroform vapor concentrations of  $p/p_{\text{sat}} = 0.25$  and 0.50 show a rapid decrease in the fwhm of the P3HT (100) diffraction peak, indicating an increase in both the scattering coherence length and the size of the crystalline domains (Figure 4b, c).<sup>60</sup> These films still show preferential face-on orientation of the P3HT, and a higher order (200) reflection appears at  $q \approx 0.71 \text{ \AA}^{-1}$  as the P3HT begins to crystallize (Figure S5). As the concentration of chloroform vapor is increased further to  $p/p_{\text{sat}} = 0.75$  and 0.95, there is only a slight reduction in the fwhm of the P3HT (100) peak, possibly due to the fwhm now being limited by instrumental broadening. However, a higher order (300) P3HT peak begins to appear at  $q \approx 1.13 \text{ \AA}^{-1}$  indicating that the P3HT continues to crystallize further. At  $p/p_{\text{sat}} = 0.95$ , the P3HT appears to be highly ordered, as evidenced by the low fwhm of the (100) P3HT peak, and the appearance of both (200) and (300) P3HT reflections. Additionally, the (100), (200), and (300) P3HT peaks become more prominent along the  $q_z$  axis, and substantially less noticeable along the  $q_r$  axis. The orthogonal (010) peak also disappears from the  $q_z$  axis, reorienting along  $q_r$ . These changes indicate a change to an edge-on orientation of the P3HT (Figure S5).<sup>4</sup> The PC<sub>61</sub>BM peak remains relatively isotropic throughout the annealing process.

**Device Performance.** To correlate the observed changes in film morphology and crystallinity to changes in OPV device performance, we prepared a series of ITO/ZnO/P3HT:PC<sub>61</sub>BM/MoO<sub>3-x</sub>/Ag devices. The P3HT:PC<sub>61</sub>BM layers were spin coated from chloroform and annealed at various chloroform vapor concentrations. The average power conversion efficiency (PCE) data are shown in Figure 5, whereas the  $J$ - $V$  curves and incident-photon-to-current-efficiency (IPCE) spectra of champion cells are plotted in Figure S6 and S7, respectively. The as cast P3HT:PC<sub>61</sub>BM devices had a relatively low PCE of  $1.6 \pm 0.1\%$  (Figure 5). Upon annealing with chloroform vapor at  $p/p_{\text{sat}} = 0.25$ , the

device efficiency increased to  $2.4 \pm 0.2\%$ . The increase in efficiency can be attributed to an increase in the short circuit current density ( $J_{\text{sc}}$ ) and a decrease in the series resistance ( $R_s$ ), resulting in a higher fill factor (FF) (Table S1). The decrease in series resistance and increase in  $J_{\text{sc}}$  are likely due to the crystallization of the P3HT (as evidenced by the UV-vis and GIWAXS data), which improves charge transport within the BHJ layer. The rate of electron transfer from donor to acceptor can also benefit from local improvements in crystallinity, and this may also contribute to the increase in  $J_{\text{sc}}$ . As the chloroform vapor concentration was increased to  $p/p_{\text{sat}} = 0.50$  and 0.75, the PCE of the devices increased to  $2.6 \pm 0.2\%$  and  $2.9 \pm 0.2\%$ , respectively. Again, the increase in PCE is driven by improvements in  $J_{\text{sc}}$  and a reduction in  $R_s$ . In contrast, the devices annealed at  $p/p_{\text{sat}} = 0.95$  showed a drop in PCE to  $2.7 \pm 0.2\%$ . The drop in PCE is due to a loss of photocurrent, for which there may be two contributing factors. First, the best performing cells in this study were those annealed at  $p/p_{\text{sat}} = 0.75$ , which displayed a bicontinuous network of donor and acceptor, with nanoscale phase separation (Figure 3). The coarser phase separation of the  $p/p_{\text{sat}} = 0.95$  annealed films (with a more globular PC<sub>61</sub>BM morphology) may be contributing to exciton recombination, reducing the rate of photocurrent generation within the device.<sup>3</sup> Second, the films annealed at  $p/p_{\text{sat}} = 0.95$  showed a strong preference for edge-on P3HT orientation; in contrast, the other films showed a greater preference for face-on orientation (Figure 4). In the edge-on orientation, the P3HT  $\pi$ -stacking direction is parallel to the substrate, enhancing in-plane charge transport at the expense of out-of-plane mobility.<sup>4</sup> Because OPV devices rely on vertical (out-of-plane) charge transport to collect photocurrent, this change in orientation might be expected to reduce the short-circuit current density.

These results show that the optimal P3HT:PC<sub>61</sub>BM morphology is one that is metastable; if overannealed, the efficiency of the device drops. A key question then becomes whether the film morphology will be stable under long-term operation, given that modules exposed to full sunlight for extended periods can reach highly elevated temperatures. We therefore performed thermal stability tests at  $80^\circ\text{C}$  on both as cast and annealed ( $p/p_{\text{sat}} = 0.75$ ) P3HT:PC<sub>61</sub>BM cells (Figure S8). The efficiency of the as cast P3HT:PC<sub>61</sub>BM devices increased from 0.9% to 2.1% over the first hour, and remained relatively stable thereafter. In contrast, the efficiency of the devices annealed at  $p/p_{\text{sat}} = 0.75$  declined rapidly (from 2.5% to 1.6%) within the first hour of thermal treatment, although it remained relatively unchanged for the remainder of the experiment. The results suggest that in the case of P3HT:PC<sub>61</sub>BM, thermally induced evolution of the film morphology may lead to a long-term decline in device performance.

**PTB7-Th:PDI-DPP-PDI. UV/Visible Spectroscopy.** Having validated the effectiveness of the VP-SVA approach in the annealing of P3HT:PC<sub>61</sub>BM active layers, we next set about determining its efficacy with more modern BHJ blends based on nonfullerene acceptors. We chose the PTB7-Th:PDI-DPP-PDI (Chart 1) system as a representative example of a less ordered donor polymer and a nonfullerene acceptor. The system was also chosen because a previous report noted that SVA could be used to increase the efficiency of PTB7-Th:PDI-DPP-PDI devices, but that overannealing led to a loss of performance;<sup>6</sup> this makes the system an ideal candidate for the VP-SVA method.

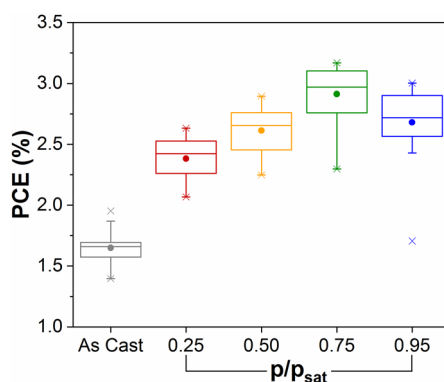


**Figure 5.** Power conversion efficiency of P3HT:PC<sub>61</sub>BM devices annealed at various chloroform concentrations. The dots represent mean values, and the central lines the medians. The box defines the 25th and 75th percentiles, whereas the bars define the 5th and 95th percentiles. The maximum and minimum PCE values are each denoted by an  $\times$ . Device statistics were derived from measurements on a minimum of 27 devices (8 devices per substrate).

We first examined neat films of the acceptor (**Figure S9**) and donor (**Figure S10**) to determine the effect of SVA on the individual components. The as cast film of PDI-DPP-PDI shows prominent PDI-based transitions at 501 and 532 nm, as well as a broad DPP-based transition at 642 nm.<sup>6</sup> After annealing at  $p/p_{\text{sat}} = 0.25$  and 0.50, there was little measurable change in the spectra; however, increasing the chloroform vapor concentration to  $p/p_{\text{sat}} = 0.75$  induced major changes to the absorbance spectrum. Both PDI-based transitions drop in intensity, with the peak at 532 nm red shifting to 539 nm; a new transition at 579 nm also replaces the broad DPP-based peak at 642 nm. This behavior is consistent with a structural rearrangement of the chromophore, most likely a change in the torsional angle between the PDI and DPP subunits. The high degree of twist within the molecular structure of PDI-DPP-PDI allows solvent vapor annealing to induce structural reorganization to a more coplanar structure, with the subsequent formation of more tightly packed dimers. This rearrangement can be correlated with the emergence of a peak in the thin-film absorption profile of PDI-DPP-PDI at 584 nm.<sup>61</sup> Increasing the chloroform vapor concentration to  $p/p_{\text{sat}} = 0.95$  further emphasizes these changes, reducing the absorbance at 501 nm and increasing the intensity of the transition at  $\sim 580$  nm. In contrast, neat films of PTB7-Th show very little response to SVA, regardless of the partial pressure of solvent vapor (**Figure S10**).

These same trends can be observed in BHJ blends of PTB7-Th:PDI-DPP-PDI (**Figure 6a** and **Figure S11**). The UV-vis spectrum of the as cast film is essentially the sum of its

components, with PDI-based peaks at 500 and 531 nm, and PTB7-Th transitions at 642 and 699 nm (which overlap with the DPP-based transition expected at 642 nm). As the films are annealed, there is little change at low chloroform vapor concentrations ( $p/p_{\text{sat}} = 0.25$  and 0.50). At  $p/p_{\text{sat}} = 0.75$ , as with pure PDI-DPP-PDI, there is a large change in the absorbance profile. The PDI-based transitions at 500 and 530 nm decrease in intensity, while a new transition grows in at 583 nm. Additionally, there is a loss of intensity between 640 and 695 nm; however, given the insensitivity of PTB7-Th to SVA (**Figure S10**), this is likely the loss of the broad DPP-based transition at 642 nm in PDI-DPP-PDI. Again, as with the neat PDI-DPP-PDI films, these changes simply become more pronounced upon annealing at  $p/p_{\text{sat}} = 0.95$ .

As with the P3HT:PC<sub>61</sub>BM films, the absorbance of a diagnostic peak (in this case, the new PDI-DPP-PDI absorbance band at 584 nm) was monitored throughout the annealing process (**Figure 6b**). The annealing experiment was conducted in the same way as before: the sample was purged with dry nitrogen for 2 min, followed by 30 min of SVA and 30 min of purging with nitrogen. Again there was a decrease in absorbance for the first  $\sim 60$  s of SVA, which is attributed to the swelling of the films. At solvent concentrations of  $p/p_{\text{sat}} = 0.25$  and 0.50, this slight drop in absorbance is the only change observed during the annealing process; it is also fully reversible, and the absorbance returns to its original value as the solvent is purged and the films dry and deswell. As with the pure PDI-DPP-PDI films, it is only after annealing at  $p/p_{\text{sat}} = 0.75$  that major structural reorganization occurs. The absorbance at 584 nm increases sharply as the solvent vapor is introduced, and increases steadily for the next 30 min of annealing. This indicates a relatively slow reorganization process relative to what was observed in the P3HT:PC<sub>61</sub>BM films. This would be consistent with the proposed rotation of large, bulky PDI subunits in the solid state, rather than the more facile interdigitation of relatively mobile alkyl chains in P3HT. Upon drying, the absorbance increases slightly as the film deswells and locks in the new PDI-DPP-PDI conformation. The same trend also occurs at  $p/p_{\text{sat}} = 0.95$ , only to a greater overall degree. Overall, the UV-vis experiments suggest that there is substantial solid state reorganization of the PDI-DPP-PDI chromophore on annealing at concentrations  $\geq 0.75$   $p/p_{\text{sat}}$ , whereas the PTB7-Th donor polymer remains relatively unchanged.

**Photoinduced Force Microscopy.** To evaluate the film morphology of the PTB7-Th:PDI-DPP-PDI blends, AFM (**Figure S12**) and PiFM (**Figure 7**) images were acquired on films, both as cast and after SVA. Unfortunately, because of the fact that PTB7-Th and PDI-DPP-PDI both contain many of the same functional groups, finding unique IR modes for PiFM analysis was challenging (**Figure S13**). The PDI-DPP-PDI could be selectively imaged by exciting carbonyl stretching modes at 1694 cm<sup>-1</sup>; however, PTB7-Th lacked any unique IR-active vibrational modes. As with the P3HT:PC<sub>61</sub>BM films, the as cast PTB7-Th:PDI-DPP-PDI sample shows a homogeneous distribution of the acceptor, with only line-scan noise evident in the image (**Figure 7**). Annealing at  $p/p_{\text{sat}} = 0.25$  or 0.50 provided little change in the film morphology, which is entirely consistent with the lack of change observed in the UV-vis spectra at these low solvent partial pressures. After annealing at  $p/p_{\text{sat}} = 0.75$ , however, there is a large change in the surface morphology. Substantial phase separation is visible in the PiFM image, with large domains of PDI-DPP-

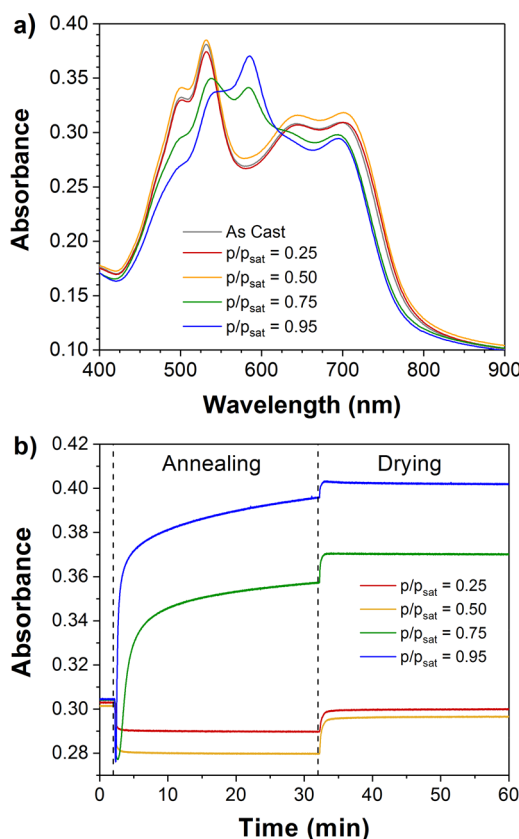


**Figure 6.** (a) Post-annealing UV-vis spectra and (b) absorbance at 584 nm as a function of time for PTB7-Th:PDI-DPP-PDI thin films annealed at various chloroform vapor concentrations.

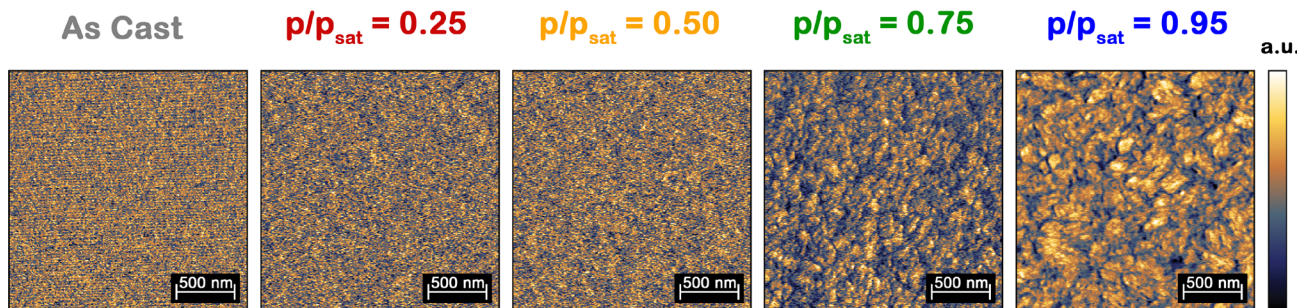


**Figure 7.** PiFM images of PTB7-Th:PDI-DPP-PDI thin films annealed at various chloroform vapor concentrations. Excitation at  $1694\text{ cm}^{-1}$ .

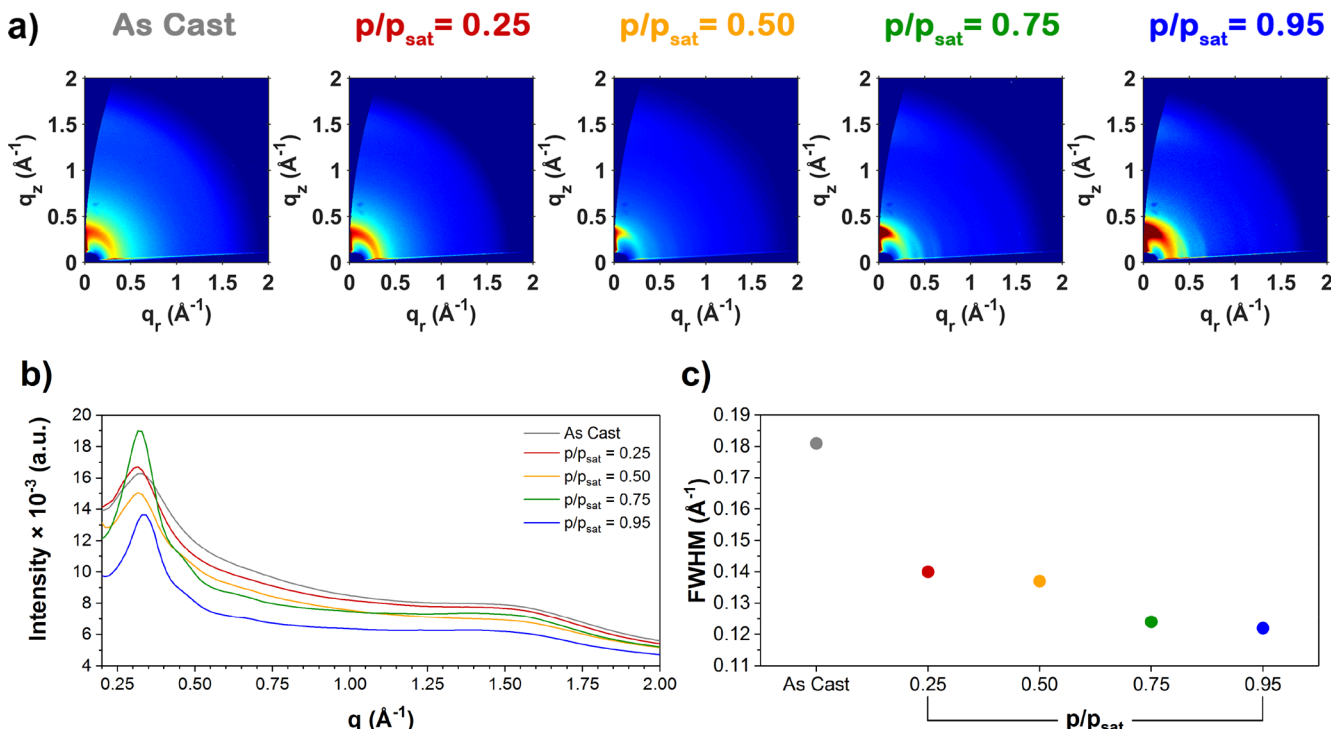


**Figure 8.** (a) GIWAXS patterns of PTB7-Th:PDI-DPP-PDI thin films annealed at various chloroform vapor concentrations. (b) Azimuthally integrated linecuts (from  $\chi = -80^\circ$  to  $80^\circ$ ) of the GIWAXS patterns from panel a. (c) fwhm of the peak at  $q \approx 0.30\text{ \AA}^{-1}$  after background subtraction.

PDI clearly evident. The degree of phase separation increases as the solvent partial pressure is increased to  $p/p_{\text{sat}} = 0.95$ ; extremely large domains of PDI-DPP-PDI are visible in the PiFM image. Importantly, the PDI-DPP-PDI domains are now on the order of 100 nm in size, suggesting that over-crystallization of the acceptor may have a deleterious impact on device performance.

These same trends can be easily visualized in the FFT of the PiFM images (Figure S14). As cast and after annealing at 0.25 and 0.50  $p/p_{\text{sat}}$  the FFT reveals a wide distribution of spatial frequencies. The only significant feature is a bias along the slow axis of the scan, again consistent with line-scan noise. After annealing at  $p/p_{\text{sat}} = 0.75$ , there is a loss of high spatial frequencies, consistent with the evolution of coarser phase domains. At the highest annealing concentration ( $p/p_{\text{sat}} = 0.95$ ), the FFT consists almost entirely of low spatial frequencies, highlighting the coarse nature of the PDI-DPP-PDI phase domains. The same trends are evident in the topographic AFM images (Figure S12). The  $R_q$  is low for the as cast film and the films annealed at  $p/p_{\text{sat}} = 0.25$  and 0.50 ( $R_q = 0.96, 0.61$ , and  $0.58\text{ nm}$ , respectively), but increases sharply

for the films annealed at  $p/p_{\text{sat}} = 0.75$  and 0.95 ( $R_q = 1.49$ , and  $2.31\text{ nm}$ , respectively). Both the UV/vis and PiFM results clearly indicate that major changes are occurring in the solid state structure of PDI-DPP-PDI during SVA, but only at chloroform partial pressures  $\geq 0.75\text{ }p/p_{\text{sat}}$ .

**Grazing Incidence Wide-Angle X-ray Scattering.** To evaluate the effect of VP-SVA on the crystallinity of the PTB7-Th:PDI-DPP-PDI active layer, we first evaluated thin films of the individual components by GIWAXS. The GIWAXS patterns of the PTB7-Th films are relatively simple (Figure S15), consisting of a lamellar (100) reflection at  $q \approx 0.26\text{ \AA}^{-1}$  (oriented along the  $q_r$  axis) and a  $\pi$ -stacking (010) peak at  $q \approx 1.59\text{ \AA}^{-1}$  (oriented along  $q_z$ ).<sup>11,62,63</sup> The angular distribution of the scattering indicates a preferential face-on orientation of the PTB7-Th, which does not change upon annealing. Notably, the scattering intensities of the reflections do not vary substantially with annealing, consistent with the less ordered nature of PTB7-Th relative to P3HT. In the GIWAXS pattern of the as cast PDI-DPP-PDI acceptor (Figure S16a), there are only two diffuse features: relatively broad rings centered at  $q \approx 0.38$  and  $1.7\text{ \AA}^{-1}$ . Given the diffuse nature of the scattering

features, they are most visible in the azimuthally integrated linecuts (Figures S16b and S17). The diffuse and relatively isotropic nature of these features suggest a weakly ordered film. There is initially little change in the GIWAXS data as the PDI-DPP-PDI films are annealed ( $p/p_{\text{sat}} = 0.25$ ); however, after annealing at  $p/p_{\text{sat}} = 0.50$ , it is clear that the PDI-DPP-PDI acceptor is beginning to crystallize. The broad peak at  $q \approx 0.38 \text{ \AA}^{-1}$  resolves into three peaks at  $q \approx 0.32, 0.46$ , and  $0.66 \text{ \AA}^{-1}$ . The fwhm of the peak at  $q \approx 0.32 \text{ \AA}^{-1}$  decreases substantially relative to the initial broad peak at  $q \approx 0.38 \text{ \AA}^{-1}$  (Figure S16c). This peak also has a slight preferred orientation toward the  $q_z$  axis. On annealing at  $p/p_{\text{sat}} = 0.75$  and  $0.95$ , the acceptor continues to crystallize further. The fwhm of the peak at  $q \approx 0.32 \text{ \AA}^{-1}$  decreases slightly, while the degree of preferred orientation increases. A new peak at  $q \approx 0.60 \text{ \AA}^{-1}$  can be resolved. This peak also shows preferred orientation. In the fully annealed sample, the diffuse ring at  $q \approx 1.7 \text{ \AA}^{-1}$  also resolves into two broad features at  $q \approx 1.5 \text{ \AA}^{-1}$  and  $1.7 \text{ \AA}^{-1}$ . The results show that initially the PDI-DPP-PDI films are mostly amorphous, and it is only after SVA at  $p/p_{\text{sat}} \geq 0.50$  that the acceptor begins to crystallize.

Having evaluated the crystallinity of the individual components, we then collected GIWAXS patterns of PTB7-Th:PDI-DPP-PDI thin films (Figure 8a). Mixing of the donor and acceptor materials breaks up the stacking of each individual component, reducing the overall crystallinity of the film. The GIWAXS patterns show a broad, relatively isotropic feature at  $q \approx 0.32 \text{ \AA}^{-1}$ , which is the sum of both PTB7-Th and PDI-DPP-PDI scattering features, and a diffuse feature centered at  $q \approx 1.5 \text{ \AA}^{-1}$  (Figure 8b). On annealing at  $p/p_{\text{sat}} = 0.25$ , there is a pronounced drop in the fwhm of the peak at  $q \approx 0.32 \text{ \AA}^{-1}$  (Figure 8c). Given the poorly ordered nature of PTB7-Th, it is likely that this is due to the crystallization of the PDI-DPP-PDI, which begins at lower partial pressures than in the neat film; this may be due to greater freedom of motion when the acceptor is suspended in the disordered polymer matrix. After SVA at  $p/p_{\text{sat}} = 0.50$ , there is an increase in the preferred orientation of the  $q \approx 0.32 \text{ \AA}^{-1}$  feature (Figure S18), while the fwhm continues to decline. Additionally, the PDI-DPP-PDI begins to diffract weakly in-plane at  $q \approx 0.43 \text{ \AA}^{-1}$  and  $0.64 \text{ \AA}^{-1}$ , as noted in the linecut along  $q_r$  (Figure S18c). At  $p/p_{\text{sat}} = 0.75$  and  $0.95$ , the fwhm of the feature at  $q \approx 0.32 \text{ \AA}^{-1}$  continues to decline, while the preferred orientation becomes more pronounced (Figure S18d,e). The in-plane scattering of the PDI-DPP-PDI acceptor becomes more pronounced, with clear peaks at  $q \approx 0.44 \text{ \AA}^{-1}$  and  $0.62 \text{ \AA}^{-1}$  along the  $q_r$  axis (Figure S18d, e). The results show that the crystallinity of the BHJ blend can be precisely tuned using the VP-SVA method, with the exact degree of crystallization of the PDI-DPP-PDI being controlled by the partial pressure of the annealing solvent vapor.

**Device Performance.** To correlate the observed changes in morphology with changes in device performance, we prepared OPV devices with PTB7-Th:PDI-DPP-PDI active layers. Fabrication procedures were performed according to the literature,<sup>6</sup> with the exception that the solvent annealing step was performed using our VP-SVA methodology. As expected, the as cast devices had a PCE of only  $1.0 \pm 0.3\%$  (Figure 9 and Table S2). As evident from the  $J-V$  curves of top-performing cells (Figure S19), the poor efficiency is due to low  $J_{\text{sc}}$  ( $3.7 \pm 0.3 \text{ mA cm}^{-2}$ ) and FF ( $28.8 \pm 0.7\%$ ). No change in PCE was observed after SVA with chloroform vapor at  $p/p_{\text{sat}} = 0.25$  (PCE =  $0.9 \pm 0.1\%$ ). Only after SVA with  $p/p_{\text{sat}} = 0.50$  did the

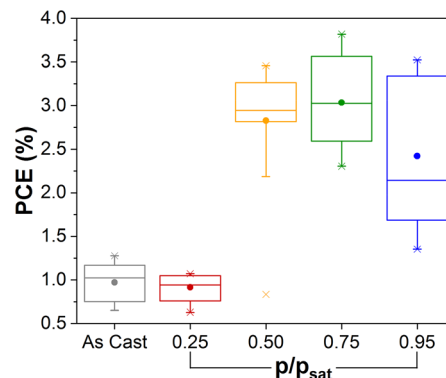


**Figure 9.** Power conversion efficiency of PTB7-Th:PDI-DPP-PDI devices annealed at various chloroform concentrations. The dots represent mean values, and the central lines the medians. The box defines the 25th and 75th percentiles, whereas the bars define the 5th and 95th percentiles. The maximum and minimum PCE values are each denoted by an  $\times$ . Device statistics were derived from measurements on a minimum of 27 devices (8 devices per substrate).

PCE increase, to  $2.8 \pm 0.6\%$ . This was due to a large increase in  $J_{\text{sc}}$  ( $7.1 \pm 0.4 \text{ mA cm}^{-2}$ ) and FF ( $41 \pm 4\%$ ). The performance at  $p/p_{\text{sat}} = 0.75$  (PCE =  $3.0 \pm 0.5\%$ ) was very similar, but dropped again after annealing at  $p/p_{\text{sat}} = 0.95$  (PCE =  $2.4 \pm 0.8\%$ ). The loss in efficiency at the highest annealing concentration is almost entirely due to a loss in photocurrent ( $J_{\text{sc}} = 6 \pm 1 \text{ mA cm}^{-2}$ ). The changes in photocurrent are reflected in the IPCE spectra (Figure S20). Additionally, the reproducibility of the PCE declined substantially at the highest chloroform partial pressures.

The observed changes in device performance can be traced back to changes in the morphology and crystallinity of the PTB7-Th:PDI-DPP-PDI active layer. Neither UV-vis, nor PiFM nor GIWAXS predict any substantial changes in film structure after annealing at  $p/p_{\text{sat}} = 0.25$ ; this is validated by the device data (Figure 9). There is, however, a substantial jump in PCE after annealing at  $p/p_{\text{sat}} = 0.50$ . Importantly, there are no substantial changes observed in the PiFM data at this annealing concentration, suggesting that this is not driven by changes in film morphology. Rather, the increase in PCE appears to be correlated to the onset of PDI-DPP-PDI crystallization, as evidenced by the appearance of new in-plane diffraction peaks at  $q \approx 0.42 \text{ \AA}^{-1}$  and  $q \approx 0.60 \text{ \AA}^{-1}$ , and a decrease in the fwhm of the feature at  $q \approx 0.32 \text{ \AA}^{-1}$  (Figure S18c). The increase in photocurrent is likely due to an increase in electron mobility within the larger acceptor crystallites.<sup>6</sup> At higher concentrations ( $p/p_{\text{sat}} = 0.75$ ), the PDI-DPP-PDI crystallization process continues (Figure S18d), leading to changes in electronic structure (Figure 6a) and the formation of discrete, phase separated domains (Figure 7). These changes increase the facility of charge transport within the active layer, leading to higher short-circuit current density, lower series resistance, and improved shunt resistance (Table S2). As the devices are overannealed ( $p/p_{\text{sat}} = 0.95$ ), however, the photocurrent drops. This is easily explained by the growth of discrete PDI-DPP-PDI domains, as visualized by PiFM (Figure 7). With phase domains well in excess of the exciton diffusion length, exciton recombination leads to fewer photogenerated charge carriers and correspondingly lower  $J_{\text{sc}}$ .

To evaluate the thermal stability of the devices, we again subjected both as cast and optimized ( $p/p_{\text{sat}} = 0.75$ ) PTB7-Th:PDI-DPP-PDI cells to 24 h of heating at  $80^{\circ}\text{C}$ . The results

are shown in Figure S21. In contrast to the P3HT:PC<sub>61</sub>BM results (Figure S8), the PTB7-Th:PDI-DPP-PDI devices changed very little with thermal treatment. The as cast devices showed a modest increase in efficiency from 1.5% to 1.8%, while the devices annealed at  $p/p_{\text{sat}} = 0.75$  were largely unchanged after 24 h of thermal treatment. This may be due to the reduced conformational flexibility in this system; as noted previously, rearrangement of the nonfullerene acceptor involves the rotation of large, bulky PDI units, as opposed to the relatively facile interdigitation of alkyl chains. This helps lock in the desired morphology of the PTB7-Th:PDI-DPP-PDI devices, making them more stable to harsh environmental conditions.

## CONCLUSION

SVA has proven to be a useful and versatile method of postdeposition processing for OPVs; however, the bell jar method lacks reproducibility and tunability. Here we have shown that a flow through VP-SVA system can be used to precisely tune the morphology of OPV active layers by controlling the chloroform vapor pressure used during the annealing process. Work on P3HT:PC<sub>61</sub>BM active layers showed that the degree of aggregation, phase separation, and crystallinity can all be controlled by varying the partial pressure of solvent vapor. The VP-SVA method was also shown to be highly applicable to more modern OPV active layers, as demonstrated by the PTB7-Th:PDI-DPP-PDI blend. Critically, both P3HT:PC<sub>61</sub>BM and PTB7-Th:PDI-DPP-PDI active layers were shown to overanneal when exposed to near-saturation ( $p/p_{\text{sat}} = 0.95$ ) solvent vapors, leading to a decline in device performance. Because the traditional bell jar SVA method relies on a solvent-saturated headspace, our results suggest that many reported OPV systems remain unoptimized.

## EXPERIMENTAL SECTION

**Materials.** All materials were used as received unless otherwise stated. Poly(3-hexylthiophene) (P3HT,  $M_w = 57000$  g/mol,  $D = 2.4$ , 91% regioregularity) was purchased from Rieke Metals. Phenyl-C<sub>61</sub>-butyric acid methyl ester (PC<sub>61</sub>BM) was purchased from Nano-C. Poly{4,8-bis[5-(2-ethylhexyl)thiophen-2-yl]benzo[1,2-b:4,5-b']dithiophene-2,6-diyl-*alt*-3-fluoro-2-[{(2-ethylhexyl)carbonyl}thieno[3,4-*b*]thiophene-4,6-diyl]} (PTB7-Th) was purchased from Luminescence Technology Inc. (Lot: S9139-170220001). PDI-DPP-PDI was synthesized according to literature procedures.<sup>6</sup> Zinc acetate dihydrate, acetone, isopropanol and chloroform were purchased from Fisher Scientific. Silver behenate, 2-methoxyethanol, and ethanolamine were purchased from Sigma-Aldrich.

**Characterization.** UV/vis spectroscopy was carried out on thin films deposited on glass substrates using a Cary 6000i spectrophotometer. In situ experiments were carried out in a custom-built, gastight aluminum chamber. Scans were performed from 900 to 250 nm at a rate of 1010 nm/min. FTIR experiments were carried out on a Bruker Alpha Platinum-ATR FTIR spectrometer. PiFM was performed on thin films on ITO/ZnO substrates using a Molecular Vista microscope. Images were acquired in sideband mode, where the PiFM and topography images were obtained at the first and second mechanical resonance frequencies of a Pt coated, Si MikroMasch cantilever (320 kHz and 1.9 MHz, respectively). Scans were acquired at 0.25–0.35 lines/s with time constants of 10–20 ms.

**GIWAXS.** GIWAXS experiments were performed at the Canadian Light Source (CLS) using the Hard X-ray MicroAnalysis (HXMA) beamline; a photon energy of 12.7 keV was selected using a Si(111) monochromator. GIWAXS patterns were collected with a SX165 CCD detector (80  $\mu\text{m}$  pixel size; 16.3 cm diameter), which was

placed 158 mm from the sample center. The beam slits were set to a 0.10 mm vertical gap and a 0.30 mm horizontal gap. Thin film samples were deposited on {100} silicon wafers with an ~100 nm thermal oxide layer, and the angle of incidence of the X-ray beam was set to 0.02°. The GIWAXS data were calibrated against a silver behenate standard and analyzed using GIXSGUI.<sup>64</sup>

**Device Characterization.** Current–voltage measurements on OPV devices were performed inside a nitrogen-filled glovebox using a Keithley 2400 source-measure unit. The cells were illuminated by a 450 W Class AAA solar simulator equipped with an AM1.5G filter (Oriel Instruments, Sol3A) at a calibrated intensity of 1 Sun, as determined by a standard silicon reference cell (Oriel Instruments, 91150 V). The cell area was defined to be 0.0708  $\text{cm}^2$  by a nonreflective anodized aluminum mask. IPCE spectra were measured in air on champion devices using a QE–PV-Si system (Oriel Instruments) consisting of a 300 W Xe arc lamp, monochromator, chopper, lock-in amplifier, and certified silicon reference cell, operating at a 30 Hz chopping frequency.

**Variable-Pressure Solvent Vapor Annealing.** VP-SVA was performed using a stream of nitrogen carrier gas connected to two Alicat MC-500SCCM-D/5 M mass flow controllers set to a combined total flow rate of 250 standard cubic centimeters per minute (SCCM). One gas stream was passed through two solvent bubblers connected in series to become saturated with solvent vapor ( $p_{\text{sat}}$ ). The second gas stream remained dry. The two gas streams were mixed, with the relative flow rates defining the partial pressure of the solvent vapor ( $p/p_{\text{sat}}$ ). All annealing experiments were performed by flowing dry nitrogen over the sample for 2 min, followed by 30 min of solvent vapor annealing and 30 min of drying under a flow of dry nitrogen.

**Substrate Preparation.** Glass substrates (Fisherbrand glass microscope slides) and {100} oriented silicon wafers (100 nm thermal oxide, University Wafer) were prepared by cutting into 25 mm × 25 mm squares, and ITO-patterned glass substrates (25 mm × 25 mm,  $R_s = 20 \Omega/\text{sq}$ ) were purchased from Xin Yan Technology Ltd. The substrates were cleaned by successive sonication for 20 min in 2% Extran detergent in distilled water, Millipore water, acetone, and isopropanol and stored under isopropanol until use. All substrates were blown dry with filtered nitrogen and UV/ozone cleaned for 15 min immediately prior to use.

**ZnO Films.** ZnO sol–gel precursor solutions were prepared by dissolving zinc acetate dihydrate (108 mg, 0.49 mmol) and ethanolamine (30  $\mu\text{L}$ , 0.50 mmol) in 2-methoxyethanol (1.0 mL) and stirring vigorously overnight. The solution was then filtered through a 0.45  $\mu\text{m}$  PTFE syringe filter; 50  $\mu\text{L}$  was spin coated onto ITO-coated glass at 5000 rpm for 60 s with an acceleration of 2500 rpm/s. The films were then annealed at 180 °C for 15 min and brought into a nitrogen-filled glovebox while still hot.

**P3HT:PC<sub>61</sub>BM Films.** P3HT:PC<sub>61</sub>BM (1:0.6 (w/w), 10 mg/mL total concentration) solutions in chloroform (dried over 4 Å molecular sieves and degassed in vacuo) were prepared inside a nitrogen-filled glovebox. The solutions were stirred overnight at room temperature, and enough solvent was added to compensate for any evaporation; the solutions were then filtered through a 0.45  $\mu\text{m}$  PTFE syringe filter and spin coated (1000 rpm for 15 s and 3000 rpm for 45 s) onto either glass/ZnO, ITO/ZnO, or silicon substrates. The films were then solvent annealed as described in the text.

**PTB7-Th:PDI-DPP-PDI Films.** Neat PTB7-Th (10 mg/mL), PDI-DPP-PDI (10 mg/mL), and 2:3 (w/w) PTB7-Th:PDI-DPP-PDI (10 mg/mL total concentration) solutions in chloroform were prepared in air. The solutions were stirred overnight at room temperature, and enough solvent was added to compensate for any evaporation; the solutions were then filtered through a 0.45  $\mu\text{m}$  syringe filter and spin coated (1500 rpm for 60 s, with an acceleration of 10000 rpm/s) onto either glass/ZnO, ITO/ZnO, or silicon substrates. The films were then solvent-annealed as described in the text.

**OPV Device Fabrication.** After depositing and annealing the ITO/ZnO/P3HT:PC<sub>61</sub>BM and ITO/ZnO/PTB7-Th:PDI-DPP-PDI films, MoO<sub>3-x</sub> (7 nm, 0.1 Å/s) and Ag (100 nm, 0.3 Å/s) were thermally evaporated at a base pressure of  $1 \times 10^{-6}$  mbar.

**Thermal Stability.** P3HT:PC<sub>61</sub>BM and PTB7-Th:PDI-DPP-PDI devices were fabricated as described above. The efficiency of as cast devices and devices annealed at a chloroform concentration of  $p/p_{\text{sat}} = 0.75$  were measured as described above, then the devices were placed on a hot plate set to 80 °C for 1 h. The devices were then allowed to cool and their efficiencies measured before the films were placed back on the hot plate. The process was repeated for 24 h with the heating time increasing in duration at later stages in the study.

## ■ ASSOCIATED CONTENT

### § Supporting Information

The Supporting Information is available free of charge on the ACS Publications website at DOI: [10.1021/acsaem.8b01214](https://doi.org/10.1021/acsaem.8b01214).

In situ UV-vis scans of BHJ films during annealing, UV-vis absorbance of neat PTB7-Th and PDI-DPP-PDI annealed at various chloroform concentrations, AFM topography of BHJ films annealed at various chloroform conditions, PiFM and FT-IR absorbance of neat OPV materials, FFT of PiFM images of BHJs annealed at various chloroform concentrations, GI-WAXS linecuts of BHJ films and GIWAXS patterns of neat PTB7-Th and PDI-DPP-PDI, JV curves and IPCE of champion devices, tables of device data and statistics, thermal stability data, photographs of the VP-SVA apparatus ([PDF](#))

## ■ AUTHOR INFORMATION

### Corresponding Author

\*E-mail: [tim.kelly@usask.ca](mailto:tim.kelly@usask.ca).

### ORCID

Jessica Kong: [0000-0003-3009-6288](https://orcid.org/0000-0003-3009-6288)

Gregory C. Welch: [0000-0002-3768-937X](https://orcid.org/0000-0002-3768-937X)

Timothy L. Kelly: [0000-0002-2907-093X](https://orcid.org/0000-0002-2907-093X)

### Author Contributions

All authors have given approval to the final version of the manuscript.

### Notes

The authors declare no competing financial interest.

## ■ ACKNOWLEDGMENTS

The Natural Sciences and Engineering Research Council of Canada (NSERC, RGPIN-2017-03732, RGPIN-2013-435715) and the University of Saskatchewan are acknowledged for financial support. D.J.Z. thanks NSERC for scholarship support. S.M.M. acknowledges NSERC and Killam Laureates for scholarship support. T.L.K. and G.C.W. are Canada Research Chairs. This research was undertaken, in part, thanks to funding from the Canada Research Chairs program. G.C.W. acknowledges a Canada Foundation for Innovation (CFI) JELF award (34102). J.K. thanks the Clean Energy Institute for financial support. A portion this work was conducted with instrumentation supported by the University of Washington Student Technology Fee at the Molecular Analysis Facility, a National Nanotechnology Coordinated Infrastructure site at the University of Washington, which is supported in part by the National Science Foundation (Grant ECC-1542101), the University of Washington, the Molecular Engineering & Sciences Institute, the Clean Energy Institute, and the National Institutes of Health. The Canadian Light Source (CLS) is supported by CFI, NSERC, the University of Saskatchewan, the Government of Saskatchewan, Western Economic Diversification Canada, the National Research Council

Canada, and the Canadian Institutes of Health Research. Technical support from HXMA beamline scientist Dr. Chang-Yong Kim is gratefully acknowledged. Prof. David S. Ginger is acknowledged for helpful discussions. Kyle Fransishyn, Nicholas Randell, and Richard Pettipas are acknowledged for assistance with the GIWAXS experiments. Tyler Moorhart, Kaiyang Tu, and Dr. Pia Wennek are acknowledged for assistance with the IR spectroscopy.

## ■ REFERENCES

- (1) Zhao, F.; Wang, C.; Zhan, X. Morphology Control in Organic Solar Cells. *Adv. Energy Mater.* **2018**, *1803147*.
- (2) Mazzio, K. A.; Luscombe, C. K. The Future of Organic Photovoltaics. *Chem. Soc. Rev.* **2015**, *44*, 78–90.
- (3) Hedley, G. J.; Ruseckas, A.; Samuel, I. D. W. Light Harvesting for Organic Photovoltaics. *Chem. Rev.* **2017**, *117*, 796–837.
- (4) Verploegen, E.; Miller, C. E.; Schmidt, K.; Bao, Z.; Toney, M. F. Manipulating the Morphology of P3HT–PCBM Bulk Heterojunction Blends with Solvent Vapor Annealing. *Chem. Mater.* **2012**, *24*, 3923–3931.
- (5) Li, G.; Shrotriya, V.; Huang, J.; Yao, Y.; Moriarty, T.; Emery, K.; Yang, Y. High-Efficiency Solution Processable Polymer Photovoltaic Cells by Self-Organization of Polymer Blends. *Nat. Mater.* **2005**, *4*, 864–868.
- (6) McAfee, S. M.; Dayneko, S. V.; Josse, P.; Blanchard, P.; Cabanetos, C.; Welch, G. C. Simply Complex: The Efficient Synthesis of an Intricate Molecular Acceptor for High-Performance Air-Processed and Air-Tested Fullerene-Free Organic Solar Cells. *Chem. Mater.* **2017**, *29*, 1309–1314.
- (7) Li, G.; Yao, Y.; Yang, H.; Shrotriya, V.; Yang, G.; Yang, Y. Solvent Annealing Effect in Polymer Solar Cells Based on Poly(3-Hexylthiophene) and Methanofullerenes. *Adv. Funct. Mater.* **2007**, *17*, 1636–1644.
- (8) Wu, F. C.; Li, Y. H.; Tsou, C. J.; Tung, K. C.; Yen, C. T.; Chou, F. S.; Tang, F. C.; Chou, W. Y.; Ruan, J.; Cheng, H. L. Synergistic Effects of Binary-Solvent Annealing for Efficient Polymer-Fullerene Bulk Heterojunction Solar Cells. *ACS Appl. Mater. Interfaces* **2015**, *7*, 18967–18976.
- (9) Li, Z.; Xu, X.; Zhang, W.; Meng, X.; Ma, W.; Yartsev, A.; Inganäs, O.; Andersson, M. R.; Janssen, R. A. J.; Wang, E. High Performance All-Polymer Solar Cells by Synergistic Effects of Fine-Tuned Crystallinity and Solvent Annealing. *J. Am. Chem. Soc.* **2016**, *138*, 10935–10944.
- (10) DeLongchamp, D. M.; Kline, R. J.; Fischer, D. A.; Richter, L. J.; Toney, M. F. Molecular Characterization of Organic Electronic Films. *Adv. Mater.* **2011**, *23*, 319–337.
- (11) Tremblet de Villers, B. J.; O'Hara, K. A.; Ostrowski, D. P.; Biddle, P. H.; Shaheen, S. E.; Chabinyc, M. L.; Olson, D. C.; Kopidakis, N. Removal of Residual Diiodooctane Improves Photo-stability of High-Performance Organic Solar Cell Polymers. *Chem. Mater.* **2016**, *28*, 876–884.
- (12) Dayneko, S. V.; Hendsbee, A. D.; Welch, G. C. Combining Facile Synthetic Methods with Greener Processing for Efficient Polymer-Perylene Diimide Based Organic Solar Cells. *Small Methods* **2018**, *2*, 1800081.
- (13) Holliday, S.; Luscombe, C. K. Low Boiling Point Solvent Additives for Improved Photooxidative Stability in Organic Photovoltaics. *Adv. Electron. Mater.* **2017**, *1700416*.
- (14) Jin, C.; Olsen, B. C.; Luber, E. J.; Buriak, J. M. Nanopatterning via Solvent Vapor Annealing of Block Copolymer Thin Films. *Chem. Mater.* **2017**, *29*, 176–188.
- (15) Sinturel, C.; Vayer, M.; Morris, M.; Hillmyer, M. A. Solvent Vapor Annealing of Block Polymer Thin Films. *Macromolecules* **2013**, *46*, 5399–5415.
- (16) Meng, B.; Fang, G.; Fu, Y.; Xie, Z.; Wang, L. Fine Tuning of the PCDTBT-OR:PC<sub>71</sub>BM Blend Nanoscale Phase Separation via Selective Solvent Annealing toward High-Performance Polymer Photovoltaics. *Nanotechnology* **2013**, *24*, 484004.

- (17) Liu, J.; Liang, Q.; Wang, H.; Li, M.; Han, Y.; Xie, Z.; Wang, L. Improving the Morphology of PCDTBT:PC<sub>70</sub>BM Bulk Heterojunction by Mixed-Solvent Vapor-Assisted Imprinting: Inhibiting Intercalation, Optimizing Vertical Phase Separation, and Enhancing Photon Absorption. *J. Phys. Chem. C* **2014**, *118*, 4585–4595.
- (18) Lv, H.; Zhao, X.; Xu, W.; Li, H.; Chen, J.; Yang, X. Improving Performance of Polymer Solar Cells Based on PSBTBT/PC<sub>71</sub>BM via Controlled Solvent Vapor Annealing. *Org. Electron.* **2013**, *14*, 1874–1881.
- (19) Vogelsang, J.; Brazard, J.; Adachi, T.; Bolinger, J. C.; Barbara, P. F. Watching the Annealing Process One Polymer Chain at a Time. *Angew. Chem., Int. Ed.* **2011**, *50*, 2257–2261.
- (20) Sun, K.; Xiao, Z.; Lu, S.; Zajaczkowski, W.; Pisula, W.; Hanssen, E.; White, J. M.; Williamson, R. M.; Subbiah, J.; Ouyang, J.; Holmes, A. B.; Wong, W. W. H.; Jones, D. J. A Molecular Nematic Liquid Crystalline Material for High-Performance Organic Photovoltaics. *Nat. Commun.* **2015**, *6*, 6013.
- (21) Sun, K.; Xiao, Z.; Hanssen, E.; Klein, M. F. G.; Dam, H. H.; Pfaff, M.; Gerthsen, D.; Wong, W. W. H.; Jones, D. J. The Role of Solvent Vapor Annealing in Highly Efficient Air-Processed Small Molecule Solar Cells. *J. Mater. Chem. A* **2014**, *2*, 9048–9054.
- (22) Lu, G.; Li, L.; Yang, X. Morphology and Crystalline Transition of Poly(3-Butylthiophene) Associated with Its Polymorphic Modifications. *Macromolecules* **2008**, *41*, 2062–2070.
- (23) Hu, S.; Dyck, O.; Chen, H.; Hsiao, Y.; Hu, B.; Duscher, G.; Dadmun, M.; Khomami, B. The Impact of Selective Solvents on the Evolution of Structure and Function in Solvent Annealed Organic Photovoltaics. *RSC Adv.* **2014**, *4*, 27931–27938.
- (24) Lan, S.; Yang, H.; Zhang, G.; Wu, X.; Chen, Q.; Chen, L.; Chen, H.; Guo, T. Importance of Solvent Removal Rate on the Morphology and Device Performance of Organic Photovoltaics with Solvent Annealing. *ACS Appl. Mater. Interfaces* **2017**, *9*, 20679–20685.
- (25) Tang, H.; Lu, G.; Li, L.; Li, J.; Wang, Y.; Yang, X. Precise Construction of PCBM Aggregates for Polymer Solar Cells via Multi-Step Controlled Solvent Vapor Annealing. *J. Mater. Chem.* **2010**, *20*, 683–688.
- (26) Chen, H.; Hsiao, Y.-C.; Hu, B.; Dadmun, M. Tuning the Morphology and Performance of Low Bandgap Polymer:Fullerene Heterojunctions via Solvent Annealing in Selective Solvents. *Adv. Funct. Mater.* **2014**, *24*, 5129–5136.
- (27) Chen, H.; Hsiao, Y.-C.; Hu, B.; Dadmun, M. Control of Morphology and Function of Low Band Gap Polymer–bis-Fullerene Mixed Heterojunctions in Organic Photovoltaics with Selective Solvent Vapor Annealing. *J. Mater. Chem. A* **2014**, *2*, 9883–9890.
- (28) Gu, X.; Gunkel, I.; Hexemer, A.; Gu, W.; Russell, T. P. An In Situ Grazing Incidence X-Ray Scattering Study of Block Copolymer Thin Films During Solvent Vapor Annealing. *Adv. Mater.* **2014**, *26*, 273–281.
- (29) Knoll, A.; Magerle, R.; Krausch, G. Phase Behavior in Thin Films of Cylinder-Forming ABA Block Copolymers: Experiments. *J. Chem. Phys.* **2004**, *120*, 1105–1117.
- (30) Albert, J. N. L.; Bogart, T. D.; Lewis, R. L.; Beers, K. L.; Fasolka, M. J.; Hutchison, J. B.; Vogt, B. D.; Epps, T. H. Gradient Solvent Vapor Annealing of Block Copolymer Thin Films Using a Microfluidic Mixing Device. *Nano Lett.* **2011**, *11*, 1351–1357.
- (31) Cavicchi, K. A.; Russell, T. P. Solvent Annealed Thin Films of Asymmetric Polyisoprene–Polylactide Diblock Copolymers. *Macromolecules* **2007**, *40*, 1181–1186.
- (32) Albert, J. N. L.; Young, W.-S.; Lewis, R. L.; Bogart, T. D.; Smith, J. R.; Epps, T. H. Systematic Study on the Effect of Solvent Removal Rate on the Morphology of Solvent Vapor Annealed ABA Triblock Copolymer Thin Films. *ACS Nano* **2012**, *6*, 459–466.
- (33) Gotrik, K. W.; Hannon, A. F.; Son, J. G.; Keller, B.; Alexander-Katz, A.; Ross, C. A. Morphology Control in Block Copolymer Films Using Mixed Solvent Vapors. *ACS Nano* **2012**, *6*, 8052–8059.
- (34) Stahl, B. C.; Kramer, E. J.; Hawker, C. J.; Lynd, N. A. Controlled Co-Solvent Vapor Annealing and the Importance of Quenching Conditions in Thin-Film Block Copolymer Self-Assembly. *J. Polym. Sci., Part B: Polym. Phys.* **2017**, *55*, 1125–1130.
- (35) Park, S.; Kim, B.; Xu, J.; Hofmann, T.; Ocko, B. M.; Russell, T. P. Lateral Ordering of Cylindrical Microdomains Under Solvent Vapor. *Macromolecules* **2009**, *42*, 1278–1284.
- (36) Zhang, J.; Posselt, D.; Sepe, A.; Shen, X.; Perlich, J.; Smilgies, D.-M.; Papadakis, C. M. Structural Evolution of Perpendicular Lamellae in Diblock Copolymer Thin Films during Solvent Vapor Treatment Investigated by Grazing-Incidence Small-Angle X-Ray Scattering. *Macromol. Rapid Commun.* **2013**, *34*, 1289–1295.
- (37) Zhang, J.; Posselt, D.; Smilgies, D.-M.; Perlich, J.; Kyriakos, K.; Jakob, S.; Papadakis, C. M. Lamellar Diblock Copolymer Thin Films during Solvent Vapor Annealing Studied by GISAXS: Different Behavior of Parallel and Perpendicular Lamellae. *Macromolecules* **2014**, *47*, 5711–5718.
- (38) Gunkel, I.; Gu, X.; Sun, Z.; Schaible, E.; Hexemer, A.; Russell, T. P. An *In Situ* GISAXS Study of Selective Solvent Vapor Annealing in Thin Block Copolymer Films: Symmetry Breaking of in-Plane Sphere Order upon Deswelling. *J. Polym. Sci., Part B: Polym. Phys.* **2016**, *54*, 331–338.
- (39) Bai, W.; Yager, K. G.; Ross, C. A. *In Situ* Characterization of the Self-Assembly of a Polystyrene–Polydimethylsiloxane Block Copolymer during Solvent Vapor Annealing. *Macromolecules* **2015**, *48*, 8574–8584.
- (40) Engmann, S.; Ro, H. W.; Herzing, A.; Snyder, C. R.; Richter, L. J.; Geraghty, P. B.; Jones, D. J. Film Morphology Evolution during Solvent Vapor Annealing of Highly Efficient Small Molecule Donor/Acceptor Blends. *J. Mater. Chem. A* **2016**, *4*, 15511–15521.
- (41) Crossland, E. J. W.; Rahimi, K.; Reiter, G.; Steiner, U.; Ludwigs, S. Systematic Control of Nucleation Density in Poly(3-Hexylthiophene) Thin Films. *Adv. Funct. Mater.* **2011**, *21*, 518–524.
- (42) Crossland, E. J. W.; Tremel, K.; Fischer, F.; Rahimi, K.; Reiter, G.; Steiner, U.; Ludwigs, S. Anisotropic Charge Transport in Spherulitic Poly(3-Hexylthiophene) Films. *Adv. Mater.* **2012**, *24*, 839–844.
- (43) Spano, F. C.; Silva, C. H. and J-Aggregate Behavior in Polymeric Semiconductors. *Annu. Rev. Phys. Chem.* **2014**, *65*, 477–500.
- (44) Clark, J.; Chang, J.-F.; Spano, F. C.; Friend, R. H.; Silva, C. Determining Exciton Bandwidth and Film Microstructure in Polythiophene Films Using Linear Absorption Spectroscopy. *Appl. Phys. Lett.* **2009**, *94*, 163306.
- (45) Vegso, K.; Siffalovic, P.; Jergel, M.; Nadazdy, P.; Nadazdy, V.; Majkova, E. Kinetics of Polymer–Fullerene Phase Separation during Solvent Annealing Studied by Table-Top X-Ray Scattering. *ACS Appl. Mater. Interfaces* **2017**, *9*, 8241–8247.
- (46) Park, J. H.; Kim, J. S.; Lee, J. H.; Lee, W. H.; Cho, K. Effect of Annealing Solvent Solubility on the Performance of Poly(3-Hexylthiophene)/Methanofullerene Solar Cells. *J. Phys. Chem. C* **2009**, *113*, 17579–17584.
- (47) Andrienko, D.; Brinkmann, M.; Daoulas, K.; Djurado, D.; Hartmann, L.; Kayunkid, N.; Ludwigs, S.; Luscombe, C. K.; Moule, A. J.; Neher, D.; Poelking, C.; Sista, P.; Tremel, K.; Troisi, A.; Turner, S. T.; Zaumseil, J. *P3HT Revisited—From Molecular Scale to Solar Cell Devices*; Ludwigs, S., Ed.; Advances in Polymer Science; Springer: Berlin, 2014; Vol. 265.
- (48) Schaffer, C. J.; Palumbiny, C. M.; Niedermeier, M. A.; Jendrzejewski, C.; Santoro, G.; Roth, S. V.; Müller-Buschbaum, P. A Direct Evidence of Morphological Degradation on a Nanometer Scale in Polymer Solar Cells. *Adv. Mater.* **2013**, *25*, 6760–6764.
- (49) Wang, W.; Guo, S.; Herzig, E. M.; Sarkar, K.; Schindler, M.; Magerl, D.; Philipp, M.; Perlich, J.; Müller-Buschbaum, P. Investigation of Morphological Degradation of P3HT:PCBM Bulk Heterojunction Films Exposed to Long-Term Host Solvent Vapor. *J. Mater. Chem. A* **2016**, *4*, 3743–3753.
- (50) McAfee, S. M.; Dayneko, S. V.; Hendsbee, A. D.; Josse, P.; Blanchard, P.; Cabanatos, C.; Welch, G. C. Applying Direct Heteroarylation Synthesis to Evaluate Organic Dyes as the Core Component in PDI-Based Molecular Materials for Fullerene-Free Organic Solar Cells. *J. Mater. Chem. A* **2017**, *5*, 11623–11633.

- (51) McAfee, S. M.; Payne, A. J.; Dayneko, S. V.; Kini, G. P.; Song, C. E.; Lee, J.-C.; Welch, G. C. A Non-Fullerene Acceptor with a Diagnostic Morphological Handle for Streamlined Screening of Donor Materials in Organic Solar Cells. *J. Mater. Chem. A* **2017**, *5*, 16907–16913.
- (52) McAfee, S. M.; Payne, A. J.; Hendsbee, A. D.; Xu, S.; Zou, Y.; Welch, G. C. Toward a Universally Compatible Non-Fullerene Acceptor: Multi-Gram Synthesis, Solvent Vapor Annealing Optimization, and BDT-Based Polymer Screening. *Sol. RRL* **2018**, *2*, 1800143.
- (53) Gu, K. L.; Zhou, Y.; Morrison, W. A.; Park, K.; Park, S.; Bao, Z. Nanoscale Domain Imaging of All-Polymer Organic Solar Cells by Photo-Induced Force Microscopy. *ACS Nano* **2018**, *12*, 1473–1481.
- (54) McLean, R. S.; Sauer, B. B. Tapping-Mode AFM Studies Using Phase Detection for Resolution of Nanophases in Segmented Polyurethanes and Other Block Copolymers. *Macromolecules* **1997**, *30*, 8314–8317.
- (55) Jovanov, V.; Yumnam, N.; Müller, A.; Gruber, M.; Wagner, V. Determining Material-Specific Morphology of Bulk-Heterojunction Organic Solar Cells Using AFM Phase Imaging. *J. Phys. Chem. C* **2017**, *121*, 9173–9180.
- (56) Nowak, D.; Morrison, W.; Wickramasinghe, H. K.; Jahng, J.; Potma, E.; Wan, L.; Ruiz, R.; Albrecht, T. R.; Schmidt, K.; Frommer, J.; Sanders, D. P.; Park, S. Nanoscale Chemical Imaging by Photoinduced Force Microscopy. *Sci. Adv.* **2016**, *2*, e1501571.
- (57) Hotta, S.; Rughooputh, S. D. D. V.; Heeger, A. J.; Wudl, F. Spectroscopic Studies of Soluble Poly(3-Alkylthienylenes). *Macromolecules* **1987**, *20*, 212–215.
- (58) Tsao, H. N.; Müllen, K. Improving Polymer Transistor Performance via Morphology Control. *Chem. Soc. Rev.* **2010**, *39*, 2372–2386.
- (59) Gargi, D.; Kline, R. J.; DeLongchamp, D. M.; Fischer, D. A.; Toney, M. F.; O'Connor, B. T. Charge Transport in Highly Face-On Poly(3-Hexylthiophene) Films. *J. Phys. Chem. C* **2013**, *117*, 17421–17428.
- (60) Patterson, A. L. The Scherrer Formula for X-Ray Particle Size Determination. *Phys. Rev.* **1939**, *56*, 978–982.
- (61) Payne, A.-J.; Rice, N. A.; McAfee, S. M.; Li, S.; Josse, P.; Cabanetos, C.; Risko, C.; Lessard, B. H.; Welch, G. C. Donor or Acceptor? How Selection of the Rylene Imide End Cap Impacts the Polarity of  $\pi$ -Conjugated Molecules for Organic Electronics. *ACS Appl. Energy Mater.* **2018**, *1*, 4906.
- (62) Al-Hussein, M.; Herzig, E. M.; Schindler, M.; Löhrer, F.; Palumbiny, C. M.; Wang, W.; Roth, S. V.; Müller-Buschbaum, P. Comparative Study of the Nanomorphology of Spray and Spin Coated PTB7 Polymer: Fullerene Films. *Polym. Eng. Sci.* **2016**, *56*, 889–894.
- (63) Chao, P.; Mu, Z.; Wang, H.; Mo, D.; Chen, H.; Meng, H.; Chen, W.; He, F. Chlorination of Side Chains: A Strategy for Achieving a High Open Circuit Voltage Over 1.0 V in Benzo[1,2-b:4,5-b']Dithiophene-Based Non-Fullerene Solar Cells. *ACS Appl. Energy Mater.* **2018**, *1*, 2365–2372.
- (64) Jiang, Z. GIXSGUI: A MATLAB Toolbox for Grazing-Incidence X-Ray Scattering Data Visualization and Reduction, and Indexing of Buried Three-Dimensional Periodic Nanostructured Films. *J. Appl. Crystallogr.* **2015**, *48*, 917–926.